High speed optical coherence microscopy with autofocus adjustment and a miniaturized endoscopic imaging probe

Aaron D. Aguirre[1,2,4], Juergen Sawinski[3], Shu-Wei Huang[1], Chao Zhou[1], Winfried Denk[3], James G. Fujimoto[1,*]

[1]*Research Laboratory of Electronics and Department of Electrical Engineering and Computer Science, Massachusetts Institute of Technology, 77 Massachusetts Avenue, Cambridge, MA 02139 USA*
[2]*Harvard-MIT Division of Health Sciences and Technology USA*
[3]*Max-Planck-Institute for Medical Research, Jahnstrasse 29, Heidelberg 69120, Germany*
[4]*aaguirre@alum.mit.edu*
[*] *jgfuji@.mit.edu*

Abstract: Optical coherence microscopy (OCM) is a promising technique for high resolution cellular imaging in human tissues. An OCM system for high-speed *en face* cellular resolution imaging was developed at 1060 nm wavelength at frame rates up to 5 Hz with resolutions of < 4 μm axial and < 2 μm transverse. The system utilized a novel polarization compensation method to combat wavelength dependent source polarization and achieve broadband electro-optic phase modulation compatible with ultrahigh axial resolution. In addition, the system incorporated an auto-focusing feature that enables precise, near real-time alignment of the confocal and coherence gates in tissue, allowing user-friendly optimization of image quality during the imaging procedure. *Ex vivo* cellular images of human esophagus, colon, and cervix as well as *in vivo* results from human skin are presented. Finally, the system design is demonstrated with a miniaturized piezoelectric fiber-scanning probe which can be adapted for laparoscopic and endoscopic imaging applications.

OCIS codes: (170.4500) Optical coherence tomography; (170.1790) Confocal microscopy; (170.2150) Endoscopic imaging

References and links

1. D. Huang, E. A. Swanson, C. P. Lin, J. S. Schuman, W. G. Stinson, W. Chang, M. R. Hee, T. Flotte, K. Gregory, C. A. Puliafito, and et, "Optical coherence tomography," Science **254**(5035), 1178–1181 (1991).
2. M. Rajadhyaksha, M. Grossman, D. Esterowitz, R. H. Webb, and R. R. Anderson, "In vivo Confocal Scanning Laser Microscopy of Human Skin: Melanin Provides Strong Contrast," J. Invest. Dermatol. **104**(6), 946–952 (1995).
3. J. A. Izatt, M. R. Hee, G. M. Owen, E. A. Swanson, and J. G. Fujimoto, "Optical coherence microscopy in scattering media," Opt. Lett. **19**(8), 590–592 (1994).
4. M. Kempe, W. Rudolph, and E. Welsch, "Comparative study of confocal and heterodyne microscopy for imaging through scattering media," J. Opt. Soc. Am. A **13**(1), 46–52 (1996).
5. J. A. Izatt, M. D. Kulkarni, H.-W. Wang, K. Kobayashi, and M. V. Sivak, Jr., "Optical coherence tomography and microscopy in gastrointestinal tissues," IEEE J. Sel. Top. Quan. Electron. **2**(4), 1017–1028 (1996).
6. A. D. Aguirre, P. Hsiung, T. H. Ko, I. Hartl, and J. G. Fujimoto, "High-resolution optical coherence microscopy for high-speed, in vivo cellular imaging," Opt. Lett. **28**(21), 2064–2066 (2003).
7. A. L. Clark, A. Gillenwater, R. Alizadeh-Naderi, A. K. El-Naggar, and R. Richards-Kortum, "Detection and diagnosis of oral neoplasia with an optical coherence microscope," J. Biomed. Opt. **9**(6), 1271–1280 (2004).
8. B. M. Hoeling, M. E. Peter, D. C. Petersen, and R. C. Haskell, "Improved phase modulation for an en-face scanning three-dimensional optical coherence microscope," Rev. Sci. Instrum. **75**(10), 3348–3350 (2004).
9. C. Xu, C. Vinegoni, T. S. Ralston, W. Luo, W. Tan, and S. A. Boppart, "Spectroscopic spectral-domain optical coherence microscopy," Opt. Lett. **31**(8), 1079–1081 (2006).
10. S. W. Huang, A. D. Aguirre, R. A. Huber, D. C. Adler, and J. G. Fujimoto, "Swept source optical coherence microscopy using a Fourier domain mode-locked laser," Opt. Express **15**(10), 6210–6217 (2007).

#120327 - $15.00 USD Received 30 Nov 2009; revised 5 Feb 2010; accepted 8 Feb 2010; published 17 Feb 2010

11. R. Huber, D. C. Adler, and J. G. Fujimoto, "Buffered Fourier domain mode locking: Unidirectional swept laser sources for optical coherence tomography imaging at 370,000 lines/s," Opt. Lett. **31**(20), 2975–2977 (2006).
12. A. Dubois, K. Grieve, G. Moneron, R. Lecaque, L. Vabre, and C. Boccara, "Ultrahigh-resolution full-field optical coherence tomography," Appl. Opt. **43**(14), 2874–2883 (2004).
13. Y. Chen, S. W. Huang, A. D. Aguirre, and J. G. Fujimoto, "High-resolution line-scanning optical coherence microscopy," Opt. Lett. **32**(14), 1971–1973 (2007).
14. F. Helmchen, M. S. Fee, D. W. Tank, and W. Denk, "A miniature head-mounted two-photon microscope. high-resolution brain imaging in freely moving animals," Neuron **31**(6), 903–912 (2001).
15. C. K. Hitzenberger, P. Trost, P. W. Lo, and Q. Y. Zhou, "Three-dimensional imaging of the human retina by high-speed optical coherence tomography," Opt. Express **11**(21), 2753–2761 (2003).
16. T. Q. Xie, Z. G. Wang, and Y. T. Pan, "High-speed optical coherence tomography using fiberoptic acousto-optic phase modulation," Opt. Express **11**(24), 3210–3219 (2003).
17. Y. C. Chen, and X. D. Li, "Dispersion management up to the third order for real-time optical coherence tomography involving a phase or frequency modulator," Opt. Express **12**(24), 5968–5978 (2004).
18. V. Westphal, S. Yazdanfar, A. M. Rollins, and J. A. Izatt, "Real-time, high velocity-resolution color Doppler optical coherence tomography," Opt. Lett. **27**(1), 34–36 (2002).
19. J. F. de Boer, C. E. Saxer, and J. S. Nelson, "Stable carrier generation and phase-resolved digital data processing in optical coherence tomography," Appl. Opt. **40**(31), 5787–5790 (2001).
20. Y. Zhao, Z. Chen, C. Saxer, S. Xiang, J. F. de Boer, and J. S. Nelson, "Phase-resolved optical coherence tomography and optical Doppler tomography for imaging blood flow in human skin with fast scanning speed and high velocity sensitivity," Opt. Lett. **25**(2), 114–116 (2000).
21. T. Q. Xie, Z. G. Wang, and Y. T. Pan, "Dispersion compensation in high-speed optical coherence tomography by acousto-optic modulation," Appl. Opt. **44**(20), 4272–4280 (2005).
22. T. Xie, D. Mukai, S. Guo, M. Brenner, and Z. Chen, "Fiber-optic-bundle-based optical coherence tomography," Opt. Lett. **30**(14), 1803–1805 (2005).
23. T. D. Wang, S. Friedland, P. Sahbaie, R. Soetikno, P. L. Hsiung, J. T. Liu, J. M. Crawford, and C. H. Contag, "Functional imaging of colonic mucosa with a fibered confocal microscope for real-time in vivo pathology," Clin. Gastroenterol. Hepatol. **5**(11), 1300–1305 (2007).
24. T. J. Muldoon, S. Anandasabapathy, D. Maru, and R. Richards-Kortum, "High-resolution imaging in Barrett's esophagus: a novel, low-cost endoscopic microscope," Gastrointest. Endosc. **68**(4), 737–744 (2008).
25. A. R. Rouse, A. Kano, J. A. Udovich, S. M. Kroto, and A. F. Gmitro, "Design and demonstration of a miniature catheter for a confocal microendoscope," Appl. Opt. **43**(31), 5763–5771 (2004).
26. C. Boudoux, S. H. Yun, W. Y. Oh, W. M. White, N. V. Iftimia, M. Shishkov, B. E. Bouma, and G. J. Tearney, "Rapid wavelength-swept spectrally encoded confocal microscopy," Opt. Express **13**(20), 8214–8221 (2005).
27. D. L. Dickensheets, and G. S. Kino, "Silicon-micromachined scanning confocal optical microscope," J. Microelectromech. Syst. **7**(1), 38–47 (1998).
28. Y. Pan, H. Xie, and G. K. Fedder, "Endoscopic optical coherence tomography based on a microelectromechanical mirror," Opt. Lett. **26**(24), 1966–1968 (2001).
29. H. Miyajima, N. Asaoka, T. Isokawa, M. Ogata, Y. Aoki, M. Imai, O. Fujimori, M. Katashiro, and K. Matsumoto, "A MEMS electromagnetic optical scanner for a commercial confocal laser scanning microscope," J. Microelectromech. Syst. **12**(3), 243–251 (2003).
30. J. M. Zara, S. Yazdanfar, K. D. Rao, J. A. Izatt, and S. W. Smith, "Electrostatic micromachine scanning mirror for optical coherence tomography," Opt. Lett. **28**(8), 628–630 (2003).
31. A. Jain, A. Kopa, Y. T. Pan, G. K. Fedder, and H. K. Xie, "A two-axis electrothermal micromirror for endoscopic optical coherence tomography," IEEE J. Sel. Top. Quan. Electron. **10**(3), 636–642 (2004).
32. W. Jung, D. T. McCormick, J. Zhang, L. Wang, N. C. Tien, and Z. P. Chen, "Three-dimensional endoscopic optical coherence tomography by use of a two-axis microelectromechanical scanning mirror," Appl. Phys. Lett. **88**(16), 163901 (2006).
33. W. Piyawattanametha, R. P. Barretto, T. H. Ko, B. A. Flusberg, E. D. Cocker, H. Ra, D. Lee, O. Solgaard, and M. J. Schnitzer, "Fast-scanning two-photon fluorescence imaging based on a microelectromechanical systems two- dimensional scanning mirror," Opt. Lett. **31**(13), 2018–2020 (2006).
34. K. C. Maitland, H. J. Shin, H. Ra, D. Lee, O. Solgaard, and R. Richards-Kortum, "Single fiber confocal microscope with a two-axis gimbaled MEMS scanner for cellular imaging," Opt. Express **14**(19), 8604–8612 (2006).
35. A. D. Aguirre, P. R. Hertz, Y. Chen, J. G. Fujimoto, W. Piyawattanametha, L. Fan, and M. C. Wu, "Two-axis MEMS scanning catheter for ultrahigh resolution three-dimensional and en face imaging," Opt. Express **15**(5), 2445–2453 (2007).
36. J. T. Liu, M. J. Mandella, H. Ra, L. K. Wong, O. Solgaard, G. S. Kino, W. Piyawattanametha, C. H. Contag, and T. D. Wang, "Miniature near-infrared dual-axes confocal microscope utilizing a two-dimensional microelectromechanical systems scanner," Opt. Lett. **32**(3), 256–258 (2007).
37. K. H. Kim, B. H. Park, G. N. Maguluri, T. W. Lee, F. J. Rogomentich, M. G. Bancu, B. E. Bouma, J. F. de Boer, and J. J. Bernstein, "Two-axis magnetically-driven MEMS scanning catheter for endoscopic high-speed optical coherence tomography," Opt. Express **15**(26), 18130–18140 (2007).
38. S. A. Boppart, B. E. Bouma, C. Pitris, G. J. Tearney, J. G. Fujimoto, and M. E. Brezinski, "Forward-imaging instruments for optical coherence tomography," Opt. Lett. **22**(21), 1618–1620 (1997).

#120327 - $15.00 USD Received 30 Nov 2009; revised 5 Feb 2010; accepted 8 Feb 2010; published 17 Feb 2010

39. M. T. Myaing, D. J. MacDonald, and X. D. Li, "Fiber-optic scanning two-photon fluorescence endoscope," Opt. Lett. **31**(8), 1076–1078 (2006).
40. A. L. Polglase, W. J. McLaren, S. A. Skinner, R. Kiesslich, M. F. Neurath, and P. M. Delaney, "A fluorescence confocal endomicroscope for in vivo microscopy of the upper- and the lower-GI tract," Gastrointest. Endosc. **62**(5), 686–695 (2005).
41. R. Kiesslich, J. Burg, M. Vieth, J. Gnaendiger, M. Enders, P. Delaney, A. Polglase, W. McLaren, D. Janell, S. Thomas, B. Nafe, P. R. Galle, and M. F. Neurath, "Confocal laser endoscopy for diagnosing intraepithelial neoplasias and colorectal cancer in vivo," Gastroenterology **127**(3), 706–713 (2004).
42. J. Sawinski, and W. Denk, "Miniature random-access fiber scanner for in vivo multiphoton imaging," J. Appl. Phys. **102**(3), 034701 (2007).
43. S. Bourquin, A. D. Aguirre, I. Hartl, P. Hsiung, T. H. Ko, J. G. Fujimoto, T. A. Birks, W. J. Wadsworth, U. Bünting, and D. Kopf, "Ultrahigh resolution real time OCT imaging using a compact femtosecond Nd:Glass laser and nonlinear fiber," Opt. Express **11**(24), 3290–3297 (2003).
44. G. J. Tearney, B. E. Bouma, and J. G. Fujimoto, "High-speed phase- and group-delay scanning with a grating-based phase control delay line," Opt. Lett. **22**(23), 1811–1813 (1997).
45. A. V. Zvyagin, E. D. Smith, and D. D. Sampson, "Delay and dispersion characteristics of a frequency-domain optical delay line for scanning interferometry," J. Opt. Soc. Am. A **20**(2), 333–341 (2003).
46. A. E. Willner, "Chromatic dispersion and polarization-mode dispersion: managing key limitations in optical communication systems," Opt. Photon. News **13**, 16–21 (2002).
47. T. M. Fortier, S. T. Cundiff, I. T. Lima, Jr., B. S. Marks, C. R. Menyuk, and R. S. Windeler, "Nonlinear polarization evolution of ultrashort pulses in microstructure fiber," Opt. Lett. **29**(21), 2548–2550 (2004).
48. Z. M. Zhu, and T. G. Brown, "Polarization properties of supercontinuum spectra generated in birefringent photonic crystal fibers," J. Opt. Soc. Am. B **21**(2), 249–257 (2004).
49. J. M. Schmitt, S. L. Lee, and K. M. Yung, "An optical coherence microscope with enhanced resolving power in thick tissue," Opt. Commun. **142**(4-6), 203–207 (1997).
50. F. Lexer, C. K. Hitzenberger, W. Drexler, S. Molebny, H. Sattmann, M. Sticker, and A. F. Fercher, "Dynamic coherent focus OCT with depth-independent transversal resolution," J. Mod. Opt. **46**, 541–553 (1999).
51. B. Qi, A. P. Himmer, L. M. Gordon, X. D. V. Yang, L. D. Dickensheets, and I. A. Vitkin, "Dynamic focus control in high-speed optical coherence tomography based on a microelectromechanical mirror," Opt. Commun. **232**(1-6), 123–128 (2004).
52. J. M. Geusebroek, F. Cornelissen, A. W. M. Smeulders, and H. Geerts, "Robust autofocusing in microscopy," Cytometry **39**(1), 1–9 (2000).

1. Introduction

Real time, *in vivo* cellular imaging of human tissues has been recognized for more than a decade as a promising application for high resolution optical microscopy methods. Current diagnosis and management of numerous human diseases, including cancers and various inflammatory and autoimmune conditions depend upon biopsy and histopathologic analysis of cellular features. Optical coherence tomography (OCT) and confocal laser scanning microscopy are two optical techniques for *in vivo* imaging of tissue microstructure [1, 2]. Imaging cells with traditional OCT methods has been difficult due to the limited transverse resolution. Confocal microscopy, on the other hand, has been shown to enable cellular resolution but has restricted imaging depth and is less amenable to development of miniaturized catheter devices due to the need for high numerical aperture optics.

Optical coherence microscopy (OCM) extends the capabilities of OCT and confocal microscopy by combining high-sensitivity, coherence-gated detection with confocal optical sectioning to improve rejection of unwanted scattered light from outside the imaging plane [3]. The improved axial sectioning provided by optical coherence gating enables greater imaging depth and contrast compared to confocal microscopy alone [3, 4]. Furthermore, by scanning an *en face* image plane with the coherence and confocal gates matched, OCM does not suffer from depth-of-field limitations present in standard depth scanning OCT and can achieve micron scale transverse image resolutions. Cellular imaging in human tissue has been demonstrated with OCM [5–7]. OCM can achieve cellular imaging in scattering tissues with lower numerical aperture compared to confocal microscopy because axial sectioning is performed with a combination of coherence and confocal gating. Using short coherence gates produced by broadband laser sources, OCM can achieve thin optical sections using coherence gating and can therefore image with lower numerical aperture [6].

#120327 - $15.00 USD Received 30 Nov 2009; revised 5 Feb 2010; accepted 8 Feb 2010; published 17 Feb 2010

Most research on *en face* OCM imaging to date has utilized time domain detection with phase modulation rather than depth scanning in the reference arm [3, 5–8]. OCM with Fourier domain detection has also been demonstrated [9, 10]. However for imaging in the *en face* plane, time domain detection can actually have an advantage in terms of speed compared with Fourier domain detection. Using Fourier domain detection, either with spectrometer-based spectral OCT or swept source OCT approaches, signals from all depths are acquired simultaneously such that an entire three-dimensional volume must be acquired in order to generate an *en face* image. This places tremendous demand on the Fourier-domain OCT system axial line rate in order to achieve high frame rates in the *en face* plane. Time domain detection, on the other hand, can acquire signals from a single *en face* plane with the reference path set to the focal depth such that only one depth is sampled at any given transverse position. As a result, image acquisition rate is determined by signal to noise constraints and by the maximum speed of the XY scanners. Because of these characteristics, time domain remains the method of choice for high speed *en face* imaging for *in vivo* applications. It should be noted, however, that advances in Fourier-domain imaging speed, particularly in swept source OCT systems, promise to make high-speed Fourier-domain OCM more available for real time imaging [11]. In addition, full-field and line-scan OCM techniques offer alternatives to traditional raster-scanning or scanning-spot OCM methods [12, 13].

To perform high resolution OCM imaging with very short coherence gates, time domain OCM systems must use high-speed, broadband reference arm phase modulators. Grating phase delay scanners have been adapted for high-speed OCM and shown to support nearly 200 nm bandwidth [6]. Using the grating phase modulator, an axial resolution of ~3 μm was achieved and high quality *in vivo* images of human skin and *Xenopus laevis* tadpole were demonstrated. A disadvantage of this modulator is the need for a rapid scanning galvanometer to generate the phase delay. This limits the modulation rate that can be achieved and requires that the lateral scan be synchronized to the modulator scanner. Synchronization can be challenging when incorporating resonant scanning devices that use *en face* scan patterns other than the standard raster scan as is typical with miniaturized scanners for endoscopic applications [14]. In addition, the grating phase modulator layout does not allow easy incorporation of a depth-scanning galvanometer to rapidly adjust the position of the coherence gate. Rapid depth scanning is necessary to perform conventional OCT and is also important for fast synchronization of the confocal and coherence gates for *in vivo* imaging.

Several groups have used acousto-optic (AO) [15–17] or electro-optic (EO) modulators [18–20] for OCT imaging. Both solutions have been shown to provide highly stable carrier frequencies suitable for phase sensitive imaging. The application of these modulators for ultrahigh coherence axial resolutions, however, requires dispersion management to compensate for the large unbalanced chromatic dispersion introduced by the modulator crystal in the reference arm [17, 21]. With appropriate dispersion compensation, AO and EO modulators offer excellent options for high-speed OCM imaging.

Development of endoscopic OCM systems for clinical imaging applications has been hindered by the lack of robust, two-axis miniaturized optical scanners, and to our knowledge, cellular-resolution endoscopic OCM images have not yet been demonstrated. Various approaches for endoscopic microscopy have been considered. Fiber-bundle arrays [22–25] allow scanning at the proximal end of the fiber bundle, which facilitates miniaturization, but they suffer from performance degradation when used with interferometric imaging methods such as OCT and OCM. Spectrally encoded scanning enables fast confocal imaging [26] but also cannot be used for OCM since it results in narrowband illumination that would destroy the axial coherence gating. Hence, the most promising approaches to date for OCM involve miniaturized distal fiber or beam scanners based on MEMS devices [27–37], piezo-electric scanners [14, 38, 39], or electromagnetic actuators [40]. A commercial fluorescence confocal endomicroscopy system has been developed using an electromagnetic balanced tuning fork and lever X-Y fiber scanner, and excellent human clinical imaging results have been

#120327 - $15.00 USD Received 30 Nov 2009; revised 5 Feb 2010; accepted 8 Feb 2010; published 17 Feb 2010

demonstrated in the gastrointestinal tract [40, 41]. This scanner in its optimized form mesasures ~5 mm in diameter and has been incorporated together with a miniaturized objective lens into a clinical endoscope. Piezo-scanners promise similar image quality and capability for miniaturization [14, 39]. Sawinski and Denk have demonstrated a novel miniaturized two-axis scanner design for *in vivo* multiphoton imaging which they have termed a piezolever fiber scanner (PLFS) [42]. This device uses paired piezo-electric bender elements in a "push-pull" configuration to achieve large optical fiber deflection and large field of view. In addition, the scanner enables non-resonant operation, which allows customized scan patterns and true random access imaging with panning and rotation [42].

This paper describes a novel time domain OCM system based on an electro-optic waveguide phase modulator for imaging at 1060 nm wavelength. The system was designed for use with a broadband Nd:Glass femtosecond laser spectrally broadened in a high numerical aperture fiber [43]. Using a modified technique from previously reported dispersion compensation approaches, the system enabled coherence axial resolutions of 3.7 μm. To allow the modulator to be used with the polarized broadband continuum, a novel polarization compensation approach was developed. In addition, a rapid linear-scanning galvanometer was incorporated into the reference arm of the system to enable fast depth scanning and precise control of the position of the coherence gate. The scanner was used to implement an algorithm for rapid, automated alignment of the optical coherence gate with the focus plane of the confocal microscope in highly scattering tissue during imaging. The algorithm was analogous to autofocusing strategies used in modern digital cameras, and its implementation ensured optimal image quality for real-time imaging. *Ex vivo* and *in vivo* cellular images acquired from human tissues with a benchtop confocal microscope are reported.

Finally, this paper demonstrates endoscopic OCM using a piezolever fiber scanner incorporated into a miniaturized package with an 8 mm outer diameter and ~60 mm rigid length. *Ex vivo* and *in vivo* cellular images were acquired at rates up to 4 Hz with <4 μm axial resolution and <2 μm transverse resolution. To our knowledge, these are the first cellular resolution OCM images of human tissue acquired with a miniaturized imaging probe.

2. OCM imaging engine

Figure 1 shows the OCM system design with a benchtop confocal microscope. A Nd:Glass femtosecond laser (HighQ Laser) generating 85 fs pulses with >165 mW output power was coupled into a 1 m length of high numerical aperture (NA) germanium-doped fiber (Nufern, UHNA3). Spectral broadening by self-phase modulation generated a >200 nm optical bandwidth centered at 1060 nm [43]. A 100 m length of single-mode fiber (Corning, HI-1060) followed the high-NA fiber before a fiber-optic 50/50 coupler and was used to broaden the femtosecond pulses to protect the electro-optic modulator from high peak intensities, as well as to reduce the peak power at the tissue sample for *in vivo* imaging. A polarization controller was included on the source input to adjust the input polarization state. The coupler divided the light between a reference arm and a sample arm, both of which also contained polarization controllers to achieve an optimized interference point spread function.

The reference arm used an electro-optic waveguide phase modulator (EOSPACE) designed for 1060 nm center wavelength. The modulator consisted of a 72 mm $LiNbO_3$ crystal and had an RF bandwidth of >12.5 GHz with low optical insertion loss <3 dB and low V_π < 5 V. Light was coupled into and out of the waveguide with polarization-maintaining (PM) optical fiber. The modulator was driven in a serrodyne fashion with a sawtooth waveform to produce a roundtrip repetitive phase swing of 2π, which resulted in an optical heterodyne frequency shift corresponding to the fundamental frequency of the drive waveform. Frequency shifts of 1-2 MHz were used depending upon the desired imaging speed. Using a pure sawtooth drive with instantaneous flyback resulted in a modulation artifact due to excitation of mechanical resonances in the modulator. The artifact was suppressed to below the system noise level by using a triangular drive waveform with a 4%

#120327 - $15.00 USD Received 30 Nov 2009; revised 5 Feb 2010; accepted 8 Feb 2010; published 17 Feb 2010

flyback time. This caused a transient in the heterodyne signal that was largely eliminated by the bandpass filter applied to the digitized signal. After the modulator, reference-arm light passed into a grating optical delay line used for dispersion compensation. The delay line also contained a rapid-depth scanning galvanometer to adjust the coherence gate.

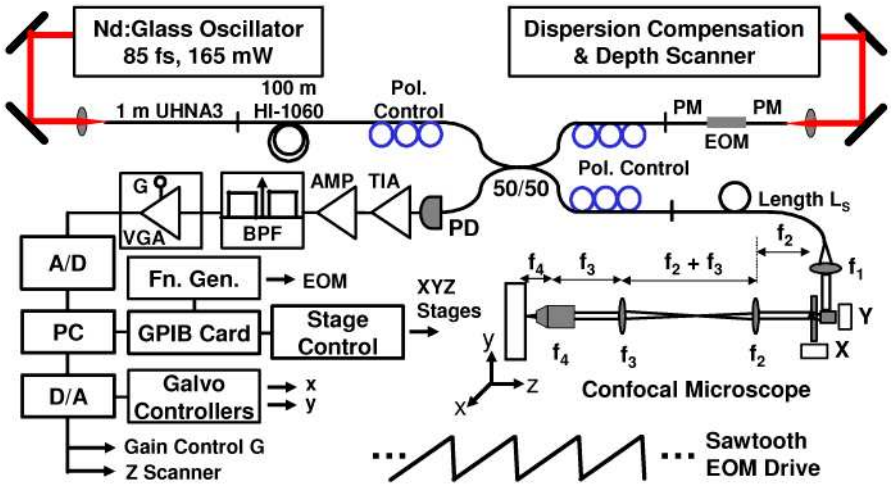

Fig. 1. High-speed OCM imaging system. The system operates at 1060 nm center wavelength using a broadband electro-optic waveguide phase modulator. TIA, transimpedance amplifier. BPF, bandpass filter. PD, photodiode. VGA, variable-gain amplifier. A/D, analog-to-digital converter. PC, personal computer. D/A, digital-to-analog converter. PM, polarization-maintaining. EOM, electro-optic modulator.

The sample arm consisted of a fiber-optic confocal microscope. The beam was collimated to a $1/e^2$ beam diameter of 1.7 mm by a custom broadband Gradium achromat (Lightpath) designed for 1060 nm. Scanning was performed using a pair of high-performance galvanometers capable of high-speed non-resonant raster scanning (Cambridge Technologies, 6215H). The scanners enabled image line rates of over 1 kHz using a triangle drive waveform and over 2.5 kHz using a sinusoidal waveform. This enabled imaging at rates of 4-8 frames per second with 500 lines/image using bidirectional acquisition. The galvanometer mirrors had 3 mm aperture. The scan lens after the galvanometers was a near-infrared achromat doublet (Edmund Optics) with 100 mm focal length. An identical doublet lens with 100 mm focal length was used as the tube lens. Finally, a 40x/0.8 NA water-immersion, plan-achromat objective lens (Zeiss Achroplan 440095) focused the beam in the specimen.

Current-to-voltage conversion was performed by a custom built, wideband transimpedance amplifier and the electrical signal was amplified by a fixed-gain stage before bandpass filtering. The filter was a cascade of a 3rd order high pass filter and a sharp 10th order low-pass anti-alias filter. The high pass cutoff was at 300 kHz and served only to remove the low-frequency incoherent intensity components to allow for fast boxcar-averaging demodulation necessary for high-speed real-time display. The anti-alias filter cutoff was set for 2.5 MHz, which corresponded to the Nyquist frequency limitation of the 5 MHz, 12 bit analog-to-digital (A/D) converter (National Instruments, 6110E). The filter had a rejection of >50 dB. A low-noise, voltage controlled variable-gain amplifier (VGA, Miteq) suitable for driving the A/D converter was used after the filter. The amplifier had a gain from 0 to 40 dB, controlled by a voltage generated by the imaging software. During imaging the gain was set to bring the maximum image intensity to the A/D maximum, allowing the full 12-bit dynamic range to be used for image digitization.

A personal computer handled data acquisition and control. The modulator driver (Agilent, 33250A) and stage controller (Newport, ESP300) were interfaced through GPIB, while the galvanometer drive signals were controlled directly by a digital-to-analog (D/A) converter.

#120327 - $15.00 USD Received 30 Nov 2009; revised 5 Feb 2010; accepted 8 Feb 2010; published 17 Feb 2010

The VGA gain control and the depth (Z) scanner were also controlled by the D/A converter. Analog-to-digital conversion of the full interference fringe signal was acquired at a 5 MHz sampling rate. Custom software was written in C++ to handle data streaming through double-buffered acquisition. For real-time imaging, images were demodulated using a fast boxcar-averaging algorithm. Offline processing for presentation used a more accurate Hilbert-transform demodulation algorithm with digital bandpass filtering and fast Fourier transform. Next, a spline resampling algorithm was applied to correct for misalignment between adjacent lines generated by bidirectional scanning. The images were also resampled to the correct aspect ratio. Following resampling, a 3x3 triangle kernel spatial filter was applied to reduce speckle effects. Finally, image compression and contrast enhancement were implemented and the images were stored in JPEG format.

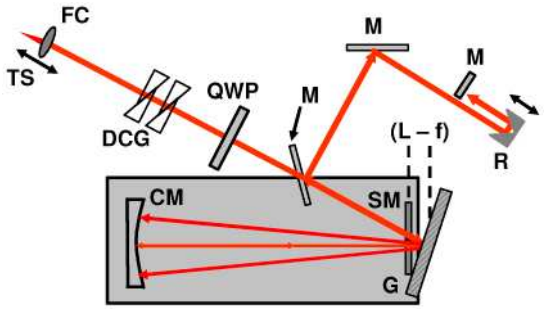

Fig. 2. Schematic of the reference arm optical delay line used for dispersion compensation and path length scanning. FC, fiber collimator. DCG, dispersion compensating glass. QWP, quarter waveplate. M, mirror. R, retroreflector. CM, curved mirror. SM, stationary mirror. G, grating.

The reference optical delay line used for dispersion compensation and depth scanning is shown in Fig. 2. The delay line was an all-reflective geometry modified from rapid scanning optical delay (RSOD) line configurations previously used for OCT and OCM [6, 44]. The grating-lens delay was used here only to compensate dispersion, but not to generate group and phase delay, and an additional linear scanning galvanometer was used for depth scanning. After collimation, the input beam was incident at ~5 degrees onto a 300 lpm grating and the first diffracted spectral order was captured by a 50 mm focal length curved mirror and focused to a stationary mirror located below the grating. Adjustment of the offset (*L-f*) between the grating and the focal plane of the curved mirror allowed adjustment of second and third-order dispersion. The linear path scanner consisted of a galvanometer with a corner cube retroreflector mounted on an arm. To improve backcoupling characteristics, the beam was focused on the final mirror in the optical path. This was achieved by double-passing the retro-reflector, since focusing on the center corner point of the retro-reflector produced large loss. Dispersion-compensating glass was introduced into the input beam path using glass blanks and adjustable prisms. In addition, a quarter-wave retarder compensated for wavelength dependent polarization properties of the source. The role of the quarter waveplate will be discussed later. The optical layout was folded to fit onto a 12” x 18” breadboard. Initial alignment of the device required careful adjustment, but once aligned, the device was robust and required little to no adjustment over weeks of operation.

The light source input bandwidth was more than 200 nm. The EOM cut the long wavelength side of the spectrum slightly, but still passed more than 190 nm. The sample arm microscope also weakly shaped the spectrum due to wavelength dependent backcoupling, although the backcoupled spectrum still measured ~200 nm. The main bandwidth limiting component in the system was the dispersion-compensating grating delay line. Because the delay line introduced large dispersion for compensation of the EOM, the ratio of $(L–f)/f$ was large and wavelength dependent backcoupling suffered as a result. The backcoupled reference arm bandwidth was 152 nm.

#120327 - $15.00 USD Received 30 Nov 2009; revised 5 Feb 2010; accepted 8 Feb 2010; published 17 Feb 2010

3. Dispersion management

To achieve broadband system operation, it was necessary to balance chromatic dispersion from the 72 mm LiNbO3 modulator crystal and the lenses in the confocal microscope. With increasing separation ($L - f$) between the grating and the focus plane of the curved mirror, increasing amounts of negative dispersion were added by the RSOD. This property was used to compensate large amounts of second order dispersion introduced by the electro-optic phase modulator [19]. Elimination of second-order dispersion, however, comes at the expense of increasing third order dispersion. Chen, et al. [17] demonstrated an elegant dispersion balancing technique which allows compensation up to third order. Adding a length, L_s, of single-mode fiber to the sample arm provided a second independent parameter that could be adjusted along with the offset ($L - f$) to zero both second and third-order dispersion mismatch. Using this method, second and third-order dispersion of the $LiNBO_3$ EOM was largely eliminated using ($L - f$) ~8 mm and L_s ~75 cm with reference arm air path length of ~92.5 cm. The RSOD settings had to be carefully adjusted empirically to achieve an optimal interference axial point spread function. The glass in the intermediate optical telescope was balanced by introducing 8 mm of SFL6 and 13 mm of LakN22. Unknown glass from additional optics was balanced by iteratively adjusting a pair of SFL6 prisms in the reference arm and the ($L - f$) offset in the grating delay line.

Typically, RSOD configurations use a fast, angular-scanning galvanometer at the Fourier plane of the grating-lens. In principle, the optical path length of the reference arm could be precisely controlled by adjusting the offset of this scanning mirror. However, in practice, three key limitations were discovered with this design. First, a much more uniform reference arm power could be obtained across the depth scan using the linear scanner in the path after the grating-lens delay unit. Second, for nonzero ($L - f$) offset, the dispersion characteristics vary across the scan [17]. This property has been used by others to compensate for depth dependent dispersion adjustment [17, 45], but was undesirable in the OCM system for this work. Finally, the angle scanner in the Fourier delay line generated an image artifact due to the resonances in the galvanometer drive circuit. Use of a slower scanner with larger inertia and lower resonances in the path after the grating unit produced a cleaner interference signal.

4. Wavelength-dependent source polarization

A disadvantage of the electro-optic modulator is that LiNbO3 is highly birefringent, with phase modulation occurring on only one polarizations. This presents problems using a polarized light source, particularly in fibers where there is polarization evolution. Previous work with electro-optic phase modulators used superluminescent diode sources that are relatively unpolarized compared to femtosecond lasers [18, 19]. For a polarized light source, it is necessary to align the field polarization with the modulator axis. Also, any spectral dependence of the polarization state results in different spectral components being modulated differently. The source used here was a linearly polarized femtosecond laser spectrally broadened in a fiber. The fiber has a small, randomly varying birefringence which can also change in time [46]. The initially linear polarization state becomes an ill-defined elliptical polarization state. Polarization evolution can also be complicated in continuum generation sources due to nonlinear polarization evolution, particularly when the pump wavelength is near the fiber zero dispersion wavelength [47, 48]. The strong wavelength dependence of polarization observed with the continuum light source requires polarization management.

Two traditional approaches were attempted to eliminate the wavelength dependence in the modulated spectrum. A commercially available achromatic depolarizer was tested, but did not scramble polarization sufficiently, resulting in fine modulation on the spectrum. A Faraday rotator was also tested in the reference-arm delay line of the OCM system after the EOM to force all wavelengths of the spectrum to see both axes of the $LiNbO_3$ modulator. The modulator was then driven with a sawtooth wave over $0 - 2V_\pi$ such that a full-wave phase

#120327 - $15.00 USD Received 30 Nov 2009; revised 5 Feb 2010; accepted 8 Feb 2010; published 17 Feb 2010

shift was acquired on single pass through the device. This worked well to remove the effects of wavelength dependent source polarization, but was limited to much less than 100 nm bandwidth, making the device unsuitable for ultrahigh axial resolution.

To overcome the bandwidth limitations of the Faraday rotator, polarization compensation was performed using a quarter-wave plate (QWP). Commercially-available achromatic zero order waveplates have several hundred nanometer bandwidths. The polarization compensation using a QWP utilizes the fact that the modulator has polarization-maintaining (PM) fiber with the fiber axes aligned to the device axes. The PM fiber ensured that the polarization states of the $LiNbO_3$ crystal were maintained until the light was launched into the reference delay line. $LiNbO_3$ has a high birefringence with the ordinary and extraordinary axis indices measuring n_o = 2.2273 and n_e = 2.1515, respectively. Over the 72 mm crystal length, this index difference produces a polarization walk-off of ~5.45 mm. This corresponds to a temporal group delay much larger than the coherence length of the light source, allowing each polarization mode to be effectively treated as a linearly polarized input wave to the reference arm. Placement of the QWP in the reference arm with its axes at 45 degrees to the PM fiber axes turned each fiber mode into a circularly polarized wave, which traveled through the delay line and back to the QWP. Upon passing back through the QWP, the wave was converted to a linear polarization again, but with an orientation orthogonal to its initial state. The QWP acted to flip the input polarization modes, forcing them back through the EOM along the opposite axis. This ensured that all wavelengths see the modulation axis of the EOM and that the polarization walk-off introduced between orthogonal crystal axes was eliminated. Note that the method did not require a specific polarization input to the PM fiber coupling into the $LiNbO_3$ modulator. The technique was insensitive to the reference arm polarization state.

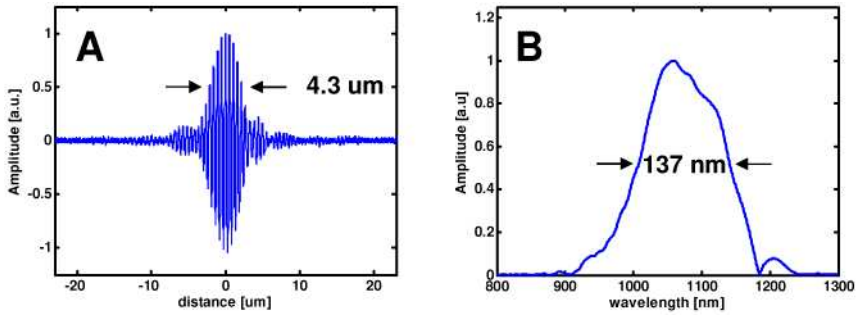

Fig. 3. Dispersion-balanced axial coherence point spread function achieved with polarization management. The axial resolution (a) measured 4.3 µm in air, corresponding to 3.1 µm in tissue. The Fourier transform of the point spread function (b), measures ~137 nm in spectral full-width at half maximum

Using this scheme in combination with the dispersion management techniques described above, the full optical bandwidth of the light source could be supported by the EOM. Figure 3(a) shows the point spread function for the dispersion balanced EOM configuration alone, without the additional glass of the confocal microscope. An axial resolution of 4.3 µm in air was achieved, which corresponds to ~ 3.1 µm in tissue (assuming a tissue index of refraction of n = 1.38). Figure 3(b) shows the corresponding bandwidth measured by Fourier transforming the interference trace. The spectral bandwidth of 137 nm was lower than the transmitted optical bandwidth of 152 nm and was due to the imperfect overlap of the backcoupled reference and sample arm fields.

The QWP polarization compensation method had a polarization-dependent image artifact. The precise etiology of the signal was not fully understood, but it was believed to be related to either a self-interfering reflection or to interference between cross-coupling components of the PM fiber axes. The artifact showed up with the characteristic frequency of the modulator

#120327 - $15.00 USD Received 30 Nov 2009; revised 5 Feb 2010; accepted 8 Feb 2010; published 17 Feb 2010

drive waveform and vanished when the modulator was not driven. However, it did not present a problem for imaging, since it could be easily and stably suppressed to below the noise level of the system by adjusting the input polarization to the OCM imaging system.

5. System performance characterization and *ex vivo* cellular imaging

Figure 4 shows the OCM instrument resolution with the benchtop microscope. Figure 4(a) shows an image of a standard 1951 USAF calibration target. The smallest elements on the target, measuring 2.2 µm wide with a periodicity of 4.4 µm were clearly visualized. Assuming a Gaussian intensity distribution, the $1/e^2$ focal spot radius was measured from the 10-90% width of an edge scan to be 1.08 µm. Moreover, the measured spot $1/e^2$ radius over a field of view of 400 x 400 µm did not exceed 1.41 µm. The microscope confocal parameter was measured by translating a mirror through the focal plane and recording the backcoupled intensity. The result (shown in Fig. 4(b)) is dz = 19 µm full-width-at-half-maximum, which corresponds to a minimum effective numerical aperture of ~0.32 based on the confocal response to a plane reflector under Gaussian beam assumptions, given as $dz = 1.4n\lambda/NA^2$. The measured coherence gate for the dispersion balanced OCM system, including the confocal microscope, is also shown in Fig. 4(b). The response measured 3.7 µm with water immersion, close to the value that would be achieved in tissue. Figure 4(b) illustrates the operating limit for this OCM instrument. The coherence gate provided the dominant axial sectioning, which operated within a relatively relaxed confocal gate. For 10 mW sample power and 350 kHz detection bandwidth, the system sensitivity measured 98 dB.

Figure 5 presents *ex vivo* images from human esophagus and colon specimens. The images were acquired in 0.5 seconds at a depth of 50 - 75 µm below the tissue surface. The field of view was 400 µm x 400 µm and the image had 500 x 500 pixels. Squamous epithelial cells and individual nuclei are visible in the esophagus image (A). The colon image(C) shows high contrast between the round crypts and inner mucous containing crypt lumens, and individual goblet cells are visible within the epithelium. The loose connective tissue lamina propria surrounding the crypts can also be clearly seen. Representative hematoxylin and eosin stained histology photos from the same specimens are shown for comparison in Fig. 5(b) and 5(d).

OCT and OCM can provide complementary information about tissue microstructure. Coregistered architectural and cellular resolution images of human cervix acquired *ex vivo* are presented in Fig. 6. Figure 6(a) shows an ultrahigh resolution OCT image of the squamous ectocervix. The squamous epithelium can be distinguished from the more highly scattering connective tissue lamina propria. Coregistered OCM cellular images taken from the same specimen are shown in Fig. 6(b) and 6(c). Cell membranes (cm) are clearly resolved (Fig. 6(b)) and an area of high signal is identified in the center of the cells which is likely from the nucleus. Deeper into the tissue, at the level of the basement membrane, a rim of highly scattering surrounds the heterogeneously scattering ridges of lamina propria. These features are better appreciated in the video provided as supplementary material in Fig. 6(b) (Media 1). The video spans from the tissue surface to a depth of 300 µm and exhibits the ability for OCM to visualize the full thickness of the epithelium well into the lamina propria.

6. Image autofocusing

Axial resolution in OCM is determined by the multiplicative effect of confocal and coherence gating. This has advantages in that it can provide stronger rejection of out of focus scattered light than either gate alone, but it also creates the unique challenge of ensuring that the gates overlap during imaging. The confocal gate position is determined by the position of the focus in the sample, while the coherence gate position is determined by the relative path

#120327 - $15.00 USD Received 30 Nov 2009; revised 5 Feb 2010; accepted 8 Feb 2010; published 17 Feb 2010

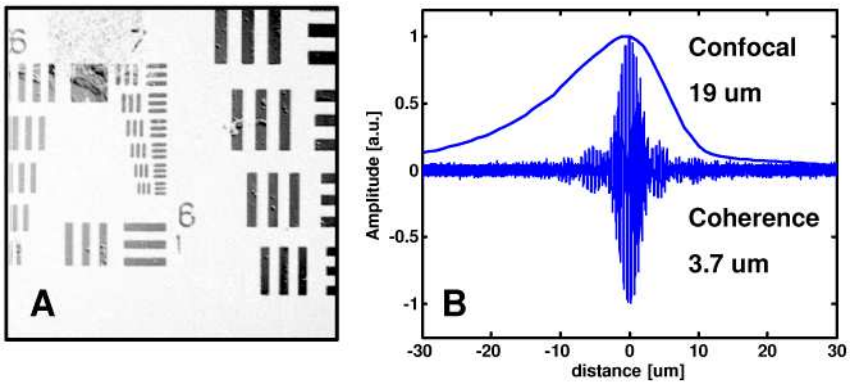

Fig. 4. Resolution characterization for the OCM instrument. High lateral resolution of <2 µm is demonstrated by the visualization of the smallest elements on the 1951 USAF resolution target (a). Overlapped confocal and coherence gates show that the dominant axial sectioning is provided by the coherence gate (b).

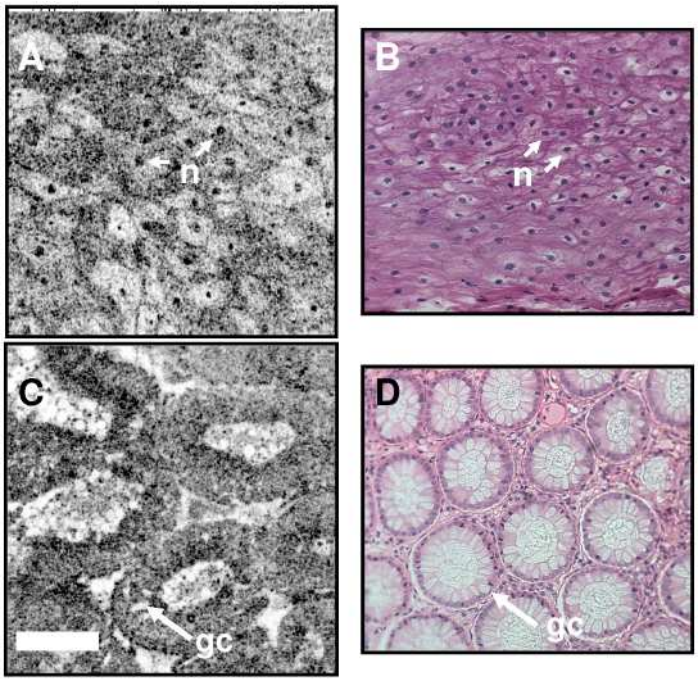

Fig. 5. *Ex vivo* OCM image of human esophagus and colon with corresponding histology. The OCM image of esophagus (a) shows cell membranes and individual nuclei in the squamous epithelium. The image of colon clearly delineates crypt architecture as well as individual goblet cells (gc) in the crypt epithelium. Correspondence with representative histology (b, d) demonstrates the ability for OCM to perform high-resolution imaging without the need for specimen processing. Notable shrinkage is evident from the OCM images of fresh tissue to the processed histology specimens. Scale bar, 100 µm.

length difference between reference and sample arms. Index of refraction differences between air and tissue and within tissue itself, as well as thermal or mechanical perturbations of the optical fiber interferometer can create relative optical path length shifts that cause the coherence and confocal gates to misalign. Gate mismatch effects are most pronounced when both the confocal and coherence gates are very narrow.

#120327 - $15.00 USD Received 30 Nov 2009; revised 5 Feb 2010; accepted 8 Feb 2010; published 17 Feb 2010

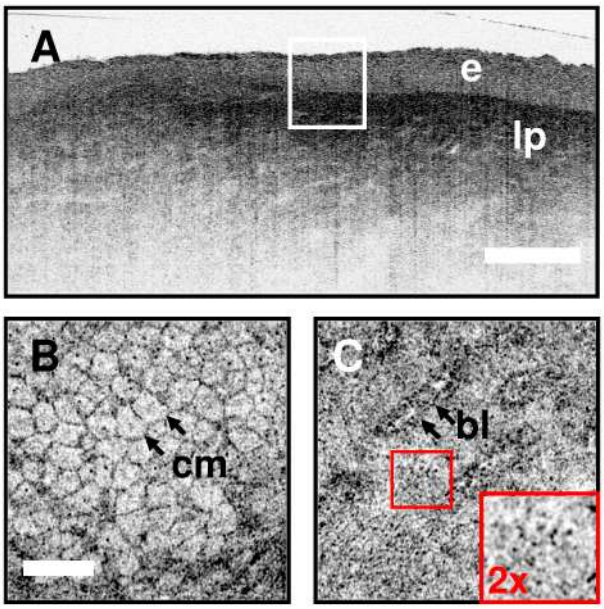

Fig. 6. Coregistered OCT and OCM images of human cervical epithelium *ex vivo*. Ultrahigh resolution OCT in (a) delineates the layered squamous epithelium (e) from the more highly scattering, heterogenous lamina propria (lp). *En face* OCM images (b, Media 1) and (c) corresponding to the region of the box in (a) demonstrate cellular and subcellular resolution below the tissue surface. Cell membranes (cm) as well as the junction between the basal layer and the underlying lamina propria (b) are distinguished. The inset in (c) demonstrates the small epithelial cells near the basal layer. The combination of OCT and OCM provides complementary information about tissue microstructure. Scale bars 500 µm (a), 100 µm (b,c). Media 1 **-** Video sequence of cellular features in human cervical epithelium *ex vivo*. Organized stratified squamous epithelial cells with progression to smaller size can be seen as the video scans from the surface to the basement membrane. Images deep into the lamina propria demonstrate the ability to image through the basement membrane into the underlying connective tissue layers

The sensitivity to gate mismatch can be reduced by broadening one of the gates, effectively enlarging the overlap region. Figure 4(b) illustrates this scenario. The wider confocal axial response provides some depth of field over which the coherence gate can operate. Use of water immersion objective lenses also limits the walk-off between the gates when focusing into tissue. For dry objective lenses, however, the coherence and confocal gates will require constant adjustment when changing depth in tissue. Moreover, fiber-optic catheters or handheld microscopes have a twisting and stretching of the optical fiber which will introduce path length shifts that can misalign the gates. Hence, a well-designed OCM system should provide a means for adjustment of the coherence gate to the location of the confocal gate in tissue. This is analogous to focusing the OCM image.

Focus-tracking techniques have been demonstrated for cross-sectional OCT imaging to scan the focus in concert with the axial depth scan [49–51]. While promising, these techniques haven't yet taken hold for OCT imaging in part due to complexity of optical design and limited flexibility for varying magnification. For *en face* OCM, most investigators have previously used a translation stage and optimized image intensity by manually setting the optical path length. This process is slow and relatively imprecise and therefore not suitable for high speed *in vivo* imaging. A more appropriate solution requires an automated adjustment of the coherence gate that can be performed rapidly during real-time imaging, analogous to autofocusing in modern digital cameras, camcorders, or light microscopes. Two general types of autofocusing have been implemented in microscopes and cameras. Active autofocusing uses an ultrasound or infrared ranging scheme to determine the distance of the object and

#120327 - $15.00 USD Received 30 Nov 2009; revised 5 Feb 2010; accepted 8 Feb 2010; published 17 Feb 2010

adjust the lens position to bring the object to focus. Passive autofocusing, conversely, utilizes iterative image processing algorithms to optimize image quality while adjusting the focus with feedback. Metrics such as image sharpness or spatial frequency content are rapidly computed to allow real time focusing [52]. The OCM system described here included the option for rapid depth adjustment using a linear-scanning galvanometer, which enabled implementation of autofocusing strategies to coordinate the positions of the confocal and coherence gates.

One strategy for OCM is to use a passive autofocusing scheme where the *en face* image sharpness is optimized while iteratively adjusting the reference path length. Another approach, analogous to active autofocusing, is to use the path scanner to perform coherence depth ranging as in cross-sectional OCT imaging. This method can be significantly faster than the passive approach because it allows direct location of the position of the confocal gate without iterative acquisition of multiple image frames. Figure 7 illustrates the principle. In Fig. 7(a), the depth scanner in the OCM system was used to acquire a lateral priority OCT image, with the lateral scan provided by the fast axis scanner in the confocal microscope. An average depth profile for the image was then generated by averaging all transverse image lines. Averaging adjacent lines eliminated effects of scattering inhomogeneities, which could lead to inaccurate estimation of the actual focal position in tissue. The depth profile effectively measures the confocal axial response in the tissue. Figures 7(c-e) show images acquired at different positions of the coherence gate relative to the confocal gate. The in-focus image in Fig. 7(d) was generated with the confocal and coherence gates exactly matched. The image in Fig. 7(c) was taken at 30 μm above the focal plane, while that in Fig. 7(e) was acquired at 30 μm below the focal plane. These out-of-focus images exhibit lower contrast and poorer resolution compared to the in-focus image, as shown in the corresponding zoom views in Fig. 7(f-h). The relative positions of the three images are shown on the depth profile in Fig. 7(b).

An autofocusing algorithm was developed using lateral-priority, cross-sectional images to locate the confocal focus. The algorithm was implemented in the OCM imaging software and enabled rapid image optimization during real-time display. Figure 8 a schematic of the algorithm. The user had the option to switch between *en face* XY imaging and cross-sectional XZ imaging modes. This allowed the user to rapidly assess the imaging depth in scattering tissue. Autofocusing could be initiated from either XZ or XY imaging mode. During autofocusing, a single XZ cross-sectional image was generated and the average depth profile computed. The reference arm depth scanner was then adjusted to coordinate the position of the coherence and confocal gates. After adjustment, the software returned to the *en face* mode. The fast algorithm required only a single frame loss from the *en face* imaging stream.

The algorithm relies on detection of the intensity peak from the focal plane, but other peaks can be generated by high backscattering outside the focal plane. The restricted confocal parameter and the averaging function across the lateral direction help to minimize this. In addition, the manual XZ viewing mode which displays the image as shown in Fig. 7(a) can be used to manually override the algorithm if a high reflection is interfering with focus detection. Furthermore, a windowing function can be used to restrict the peak search of the intensity profile around the focus to eliminate the impact of reflectors far from the true intensity peak.

7. *In vivo* cellular imaging results

To demonstrate the capability to the OCM system for high speed, *in vivo* cellular imaging, images of normal human skin were acquired from healthy volunteers. Informed consent was obtained in accordance with approved protocol on file with the Committee on the Use of Humans as Experimental Subjects (COUHES) at the Massachusetts Institute of Technology. Imaging was conducted in the nailfold region of the index finger and on the ventral forearm using a coverslip and water immersion. A ring and template device similar in principle to those used for confocal microscopy was used to stabilize the area being imaged. Images were

#120327 - $15.00 USD Received 30 Nov 2009; revised 5 Feb 2010; accepted 8 Feb 2010; published 17 Feb 2010

acquired at 5 frames per second using a line rate of 2.5 kHz and pixel sampling of 500 x 500 pixels across a field of view of 350 µm x 350 µm. Incident power measured ~10 mW at the tissue surface.

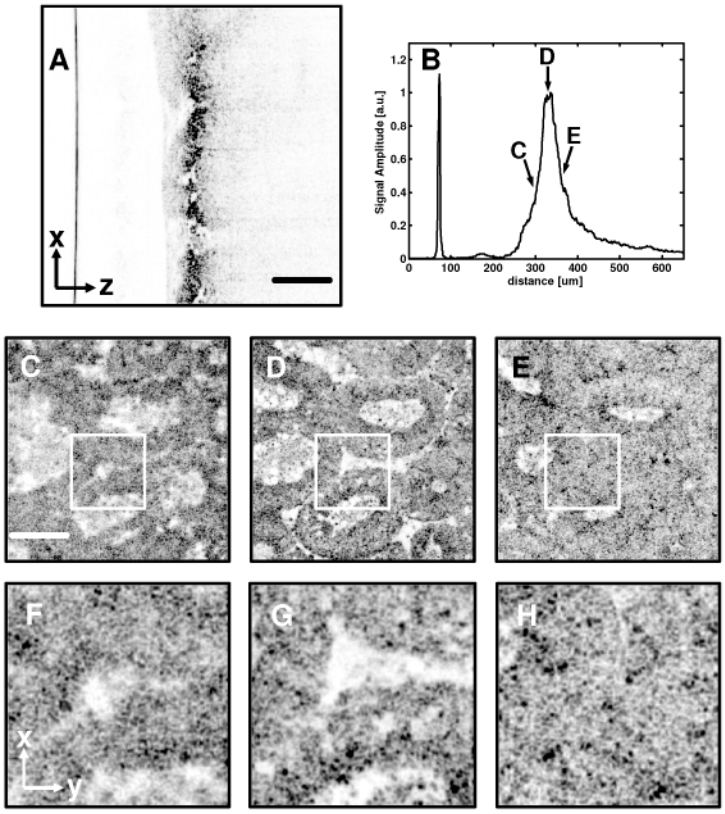

Fig. 7. Measurement of confocal gate position in scattering tissue using coherence ranging. The OCM depth scanner was used to acquire a lateral priority cross-sectional image, which clearly shows the restricted depth of field resulting from high NA focusing (A). Averaging across lateral scans produced an average depth response, which is a measure of the confocal axial response in scattering tissue (B). Images obtained with the coherence and confocal gates misaligned (C,F and E,H) appear out of focus compared to the image obtained with the gates precisely aligned (D,G). Scale bars, 100 µm.

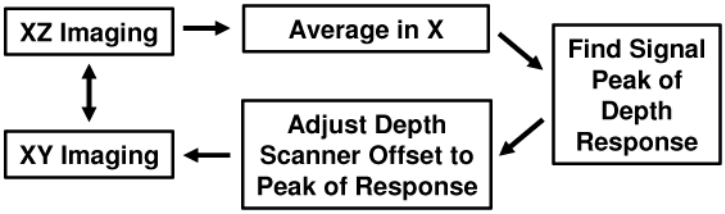

Fig. 8. Algorithm for fast autofocusing in scattering tissues.

Figure 9 shows representative imaging results from the nailfold region. The nailfold is a relatively thick region of skin compared to the ventral forearm and was selected to illustrate the OCM system imaging depth. A progression through the various layers of the skin is shown in Fig. 9(a) thru 9(c), beginning with the uppermost layer of stratum corneum. The junction between the stratum corneum and the epidermis can be readily seen in Fig. 9(c). Within the stratum corneum, thin fragments of highly scattering corneocytes are visible.

#120327 - $15.00 USD Received 30 Nov 2009; revised 5 Feb 2010; accepted 8 Feb 2010; published 17 Feb 2010

Squamous cells in the epidermis are readily visualized in Fig. 9(d) thru 9(f). The cells have strongly scattering borders, but the nuclei are not regularly visible. Ridges marking the transition between the epidermis and papillary dermis are seen in Fig. 9(f) and 9(g), while heterogeneous structure deep into the dermis is seen in Fig. 9(h) and 9(i). The sequence of images was acquired over a depth range from the surface to a depth of ~400 µm.

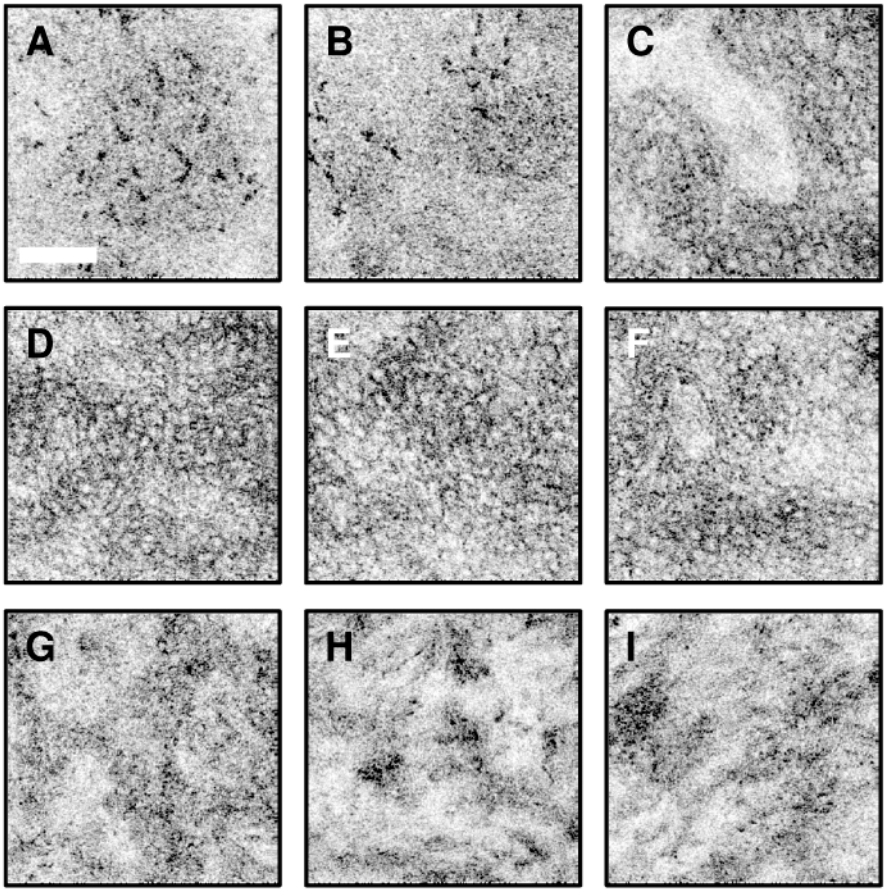

Fig. 9. *In vivo* cellular resolution OCM images of human skin. A progression is shown from the stratum corneum (a-c) thru the epidermis (d-f) and into the dermis (g-i). Highly scattering corneocytes, c, are visible in the stratum corneum in images (a) and (b) while epidermal cells become evident in images (c-f). The transition regions between the stratum corneum and the epidermis and between the epidermis and the dermis can be appreciated in (c) and (g), respectively. Scale bar, 100 µm. Image depths range from the surface to approximately 400 µm below the surface.

8. Endoscopic optical coherence microscopy

Endoscopic OCM promises to enable high speed cellular imaging *in vivo* without the need for exogenous contrast enhancing dyes. This method could have broad applications for imaging of neoplasia in the gastrointestinal and genitourinary tracts as well as in open-field surgical imaging. Furthermore, endoscopic OCM can be combined with endoscopic OCT approaches to image tissue architectural morphology over large fields of view as well as cellular features. As previously described, the lack of miniaturized two-axis scanners has limited the development of endoscopic OCM systems. In this paper, we demonstrate a piezolever fiber scanner (PLFS) similar to that previously described by Denk and Sawinski [42]. In their earlier work, the PLFS unit was incorporated into a miniature multiphoton microscope with

#120327 - $15.00 USD Received 30 Nov 2009; revised 5 Feb 2010; accepted 8 Feb 2010; published 17 Feb 2010

folded beampath designed for head-mounted small animal imaging. Here, we incorporate the PLFS unit into an inline configuration suitable for endoscopic applications.

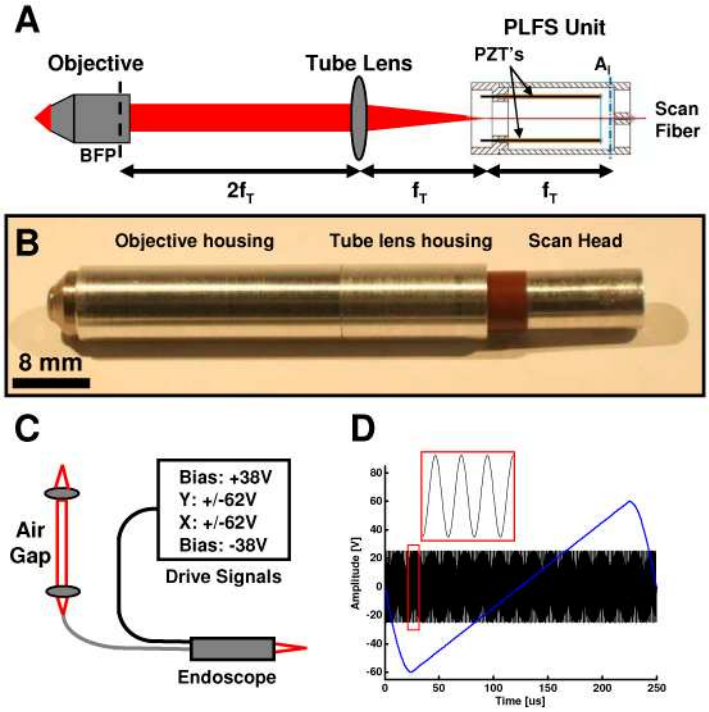

Fig. 10. Endoscope for OCM imaging. (a) Optical design. Tube lens focal length, f_T. Back focal plane, BFP. Piezoelectric actuators, PZT's. Illumination aperture, A_I. (b) Endoscope package. (c) Sample arm containing the endoscope unit, air gap coupling, and drive electronics. (d) Scanner drive waveforms.

Figure 10 shows the endoscopic OCM device. The detailed PLFS design is described in reference [42]. Briefly, the PLFS has two pairs of 2 x 10 mm trimorph piezo elements mounted in a "push-pull" configuration with the optical fiber mounted in the center of the piezo array using cross connects. The pairs are mounted orthogonally, with each pair providing a single independent scan axis. The piezo elements are biased with +/– 38V and driven between +/– 62 V. The axes are identical and can be used interchangeably. The scanner had resonances at 685 Hz and 695 Hz in the two axes. Importantly, the scanner operates in nonresonant mode, which allows programming of custom scan patterns and image rotation. The scanner can also be operated with an offset on one of the axes, to allow image panning. The scanner used a single-mode HI-1060 fiber, which was angle cleaved to minimize backreflections. The PLFS scan head was 6.4 mm in diameter and had a rigid length of 16.7 mm. The fiber pivot point which marks the device aperture was ~12.7 mm from the fiber tip.

The PLFS scanner was incorporated into an endoscope package with a tube lens and a miniaturized water-immersion, infinity-corrected microscope objective. Figure 10(a) illustrates the optical layout. The tube lens was 6.35 mm in diameter and 12.7 mm focal length. The microscope objective (Throl Optische Systeme, Germany) was 7 mm in outer diameter, 11 mm long and had 3 mm focal length and a 0.7 mm working distance. The NA was 0.9, however, the objective was underfilled and had an effective NA of ~0.5. The optical layout was a 4f imaging configuration, with the illumination aperture located 12.7 mm from the fiber tip, which was at the focal plane of the tube lens. The tube lens was 2 focal lengths, or 25.4 mm, from the objective lens back focal plane. This design enabled telecentric

#120327 - $15.00 USD Received 30 Nov 2009; revised 5 Feb 2010; accepted 8 Feb 2010; published 17 Feb 2010

scanning about a single pivot point in the back focal plane of the objective. Figure 10(b) shows the endoscope package. The housing measures 8 mm in outermost diameter by 60 mm in rigid length. The optical fiber and electrical wiring to the scanner are not shown in the photo.

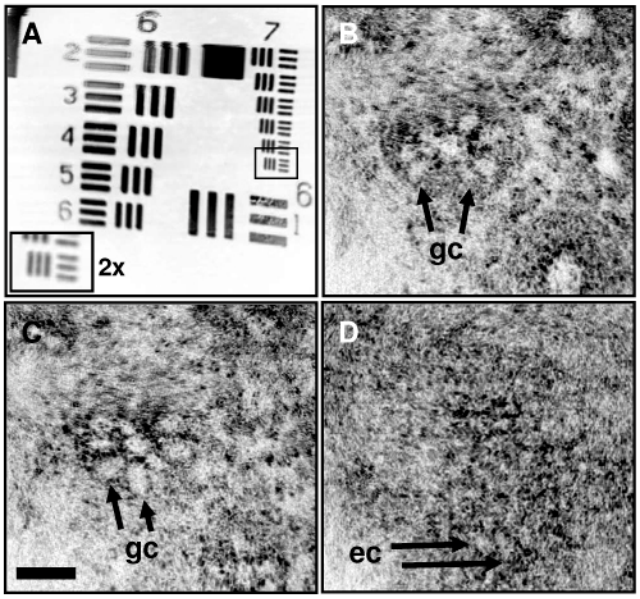

Fig. 11. Endoscopic OCM imaging. (a) USAF target demonstrating scan field of view and lateral resolution <2 µm. (b,c) *Ex vivo* images of human colon acquired at 2 frames per second. Goblet cells, gc. (d) *In vivo* image of human skin acquired at 4 frames per second. Epidermal cells, ec. Scale bar, 50 µm.

The endoscope replaced the benchtop sample arm confocal microscope in the OCM system in Fig. 1. Figure 10(c) shows the sample arm with the miniaturized scanner. An air gap coupling element was used to match the path length of the reference arm and facilitate interchange between the benchtop microscope and endoscope. The RSOD parameters were then adjusted to balance dispersion, as described previously. The optimized depth resolution for the endoscope was <4 µm in tissue. Power amplifiers with gain of 25x provided the piezo drive signals as shown in Fig. 10(d). To avoid excitation of fiber resonances due to hysteresis of the piezo elements, a raster scan pattern was used with a fast-axis sinewave drive with +/– 25 V at a frequency of 600 Hz. The slow axis drive was an asymmetric triangle wave with +/– 60 V amplitude and 2-4 Hz frequency. The triangle wave had a 80% linear ramp followed by 20% sinewave return. Image processing included resampling of the fast axis to correct for the nonlinearity of the sinusoidal drive waveform.

Figure 11 shows imaging results with the OCM endoscope. The USAF resolution target is shown in Fig. 11(a). The field of view measures 242 µm x 260 µm and the smallest elements of the target measuring 4.4 µm spacing are clearly resolved, corresponding to a transverse resolution of <2 µm. The scan field also shows minimal distortion since the axes have minimal coupling. *Ex vivo* images of freshly excised human colon acquired at 2 frames per second are shown in Fig. 11(b) and 11(c). Crypts are clearly identified with goblet cells radiating outward from the central crypt lumen. Finally, Fig. 11(d) presents *in vivo* images of human skin acquired at 4 frames per second. Epithelial cells in the epidermis are visualized.

This initial demonstration highlights the capability for cellular resolution endoscopic OCM using miniaturized scanner technology. The PLFS technology provides an excellent option for future endoscopic devices for OCM as well as three-dimensional OCT imaging. The device outer diameter can be further miniaturized through additional engineering of the

#120327 - $15.00 USD Received 30 Nov 2009; revised 5 Feb 2010; accepted 8 Feb 2010; published 17 Feb 2010

PLFS unit as well as selection of smaller-diameter lenses. It is expected that a unit with diameter <5 mm can be achieved which could potentially be used through a large diameter endoscope working channel or could be integrated into the endoscope head, similar to devices used for confocal fluorescence microscopy [40]. Future work must also consider how to perform depth scanning, waterproofing and *in vivo* safety considerations. With the availability of miniaturized scan technologies, endoscopic OCM promises to be an important advance in endoscopy and in laparoscopic surgical imaging of early cancerous conditions.

9. Conclusions

A high speed OCM system was demonstrated for *ex vivo* and *in vivo* imaging of human tissues. A femtosecond laser and continuum light source achieved coherence axial resolutions of <4 μm. Dispersion and polarization compensation were implemented to enable fast phase modulation using an electro-optic phase modulator. The system design will scale to very high imaging speeds, limited by the maximum rate of the beam raster-scanning apparatus. In addition, the system utilized a fast autofocusing technique to ensure optimal alignment of the optical coherence gate with the focal plane of the confocal microscope. The autofocusing technique will enable robust operation *in vivo* with a variety of imaging probes. High quality *ex vivo* and *in vivo* cellular images of human tissue was demonstrated with a benchtop fiber-optic confocal scanning microscope. OCM was also demonstrated using a miniaturized endoscope based on a novel piezolever fiber scanner (PLFS) technology. The device achieved comparable performance to the benchtop microscope and visualized cellular features in *ex vivo* human colon and *in vivo* human skin.

Optical coherence microscopy is an exciting extension of OCT that promises to advance several key clinical applications, including early cancer detection. OCM is particularly important for further study because of its compatibility with miniaturized device designs necessary for endoscopic and laparoscopic applications. OCM can enable high resolution endoscopic cellular imaging without the need for exogenous stains required with confocal fluorescence technologies.

Acknowledgements

This work was supported by in part by the National Institutes of Health R01-CA75289-13 and R01-EY11289-25, the Air Force Office of Scientific Research FA9550-07-1-0101 and FA9550-07-1-0014, and the Max-Planck Society. A.D. Aguirre was supported by fellowship funding from the National Institutes of Health (F31 EB005978).

#120327 - $15.00 USD Received 30 Nov 2009; revised 5 Feb 2010; accepted 8 Feb 2010; published 17 Feb 2010